Progress In Electromagnetics Research, Vol. 186, 1–10, 2026
PIER

(Received 28 April 2026, Accepted 6 July 2026, Scheduled 5 August 2026)

Revisiting Ghost Waves with Transformation Optics

Shanshan Jie[1], Wen Xiao[2,*], and Huanyang Chen[1,*]

[1] *Department of Physics, Xiamen University, Xiamen 361005, China*
[2] *College of Science, Shantou University, Shantou 515063, China*

ABSTRACT: Ghost surface polaritons (GSPs) in anisotropic materials exhibit an unusual bi-state nature with a complex-valued out-of-plane wavevector, providing unique opportunities for nanoscale light manipulation. However, the exploration and application of GSPs have been limited by the scarcity of natural crystals. Here, we revisit GSPs from the perspective of transformation optics. By introducing a shift parameter, we establish a mapping between material tensors and ghost modes, demonstrating the existence of GSPs at various transformed uniaxial interfaces. It is further shown that the wavefront can be modulated via shift parameters, enabling precise control of GSP propagation. Our study provides new insight into GSPs and establishes a versatile framework for their flexible manipulation.

1. INTRODUCTION

Polaritons in anisotropic materials have recently attracted considerable attention because of their exotic optical properties. Among them, polaritons in two-dimensional van der Waals materials exhibit extremely strong field localization, extremely long lifetimes, and directional propagation characteristics [1–9]. These unique characteristics enable a broad array of applications, such as super-resolution imaging and focusing [10–17], twisted nano-optics [18–23], nanocavities [24–27] and waveguiding [28–31], among others. At the same time, they can also be modulated by the material thickness [1], edges, and electric fields [29, 30]. The in-plane anisotropy and electronic properties of certain van der Waals materials give rise to elliptical and hyperbolic polariton dispersions, with the latter leading to an enhanced density of optical states and directional polariton propagation. For example, in α-phase molybdenum trioxide (α-MoO_3), where the in-plane permittivities have opposite signs, polaritons exhibit anomalous concave wavefronts and ray-like propagation along the material surface, with lifetimes of up to 8 picoseconds [3].

Polaritons can generally be classified as volume-confined polaritons [1, 5] and surface-confined polaritons [11, 28]. Volume-confined polaritons propagate inside low-loss crystals with a purely real-valued out-of-plane wavevector. In contrast, surface polaritons, which have a purely imaginary out-of-plane wavevector, propagate along the crystal surface and decay exponentially away from the interface. Recently, a novel type of polariton, known as ghost surface polaritons (GSPs), was reported in the classic birefringent crystal calcite [31]. In contrast to conventional surface and bulk waves, GSPs are characterized by a complex-valued normal propagation constant in an anisotropic medium. When the optical axis of calcite is slanted relative to the interface, the polaritons exhibit a unique bi-state nature, being both propagating and evanescent within the crystal bulk, which resembles the theoretically predicted "ghost waves" at the interfaces [32, 33]. They also exhibit in-plane hyperbolic characteristics similar to those of polaritons in α-MoO_3. In addition, they exhibit deep-subwavelength confinement and long-distance (over 20 micrometres) propagation [31], offering greater opportunities for light guiding using readily available natural bulk crystals.

Although GSPs show great potential in areas such as subwavelength photonics, sensing, and energy localization, these polariton modes have only been observed in a few natural crystals, such as calcite [31]. This material limitation has become a major obstacle to exploring their underlying physical mechanisms and realizing practical devices based on them. To address this limitation, we use transformation optics to design anisotropic media that can support GSPs, thereby expanding the possibilities for their realization and application. Transformation optics provides powerful tools for manipulating light fields [34, 35], and enabling the design of advanced devices [36–38], such as invisibility cloaks [39], field rotators [40, 41], concentrators [42], illusion-optics systems [43–46], and waveguide structures [47, 48].

In this study, we revisit GSPs from the perspective of transformation optics and show that they can be supported and manipulated at the interfaces of transformed uniaxial media. Furthermore, based on the analytical surface-mode solutions in the transformed medium, we derive algebraic conditions for the existence of GSPs and establish a mapping between transformed material parameters and the GSP existence domains. We also investigate the influence of the shift parameters introduced by transformation optics on the GSP wavefront within the medium and provide explicit analytical expressions. This study offers a design concept and technical approach to realize the directional manipulation of subwavelength light propagation.

* Corresponding authors: Wen Xiao (xiaowen@stu.edu.cn); Huanyang Chen (kenyon@xmu.edu.cn).

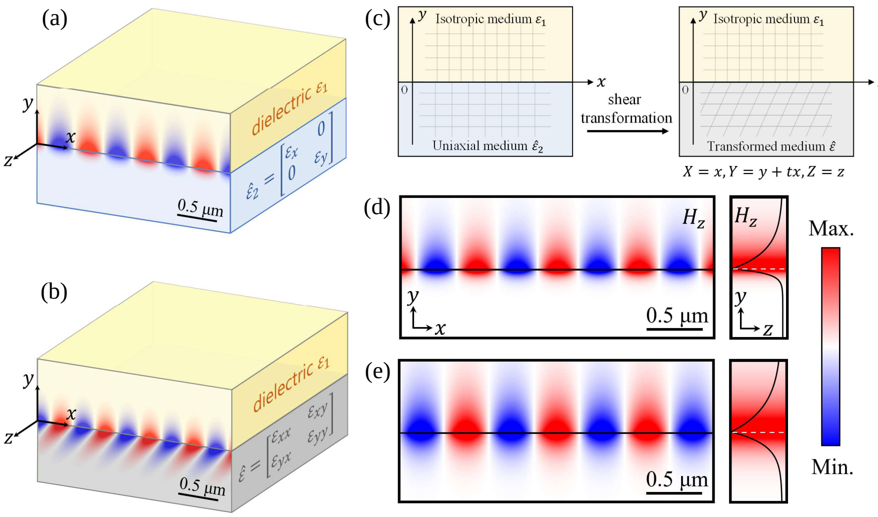

FIGURE 1. (a) Schematic of the untransformed surface-wave geometry at the interface between an isotropic medium and a uniaxial medium with a diagonal permittivity tensor. (b) Schematic of the transformed surface-wave geometry, where the lower medium is represented by an effective low-symmetry permittivity tensor with off-diagonal components. (c) Schematic illustration of the half-space shear transformation. (d) and (e) Cross-sectional near-field distribution, $\mathrm{Re}(H_z)$, of surface modes propagating along the interfaces between air and untransformed uniaxial media at $y = 0$, corresponding to $t = 0$. These modes are surface-bound but do not exhibit the simultaneous oscillation and attenuation required for GSPs. (d) shows the uniaxial metal medium ($\varepsilon_x = -4$, $\varepsilon_y = -1$), (e) shows the Type-II uniaxial hyperbolic medium ($\varepsilon_x = -2$, $\varepsilon_y = 4$). The solid black lines in (d)–(e) denote the air-medium interfaces.

2. MODEL AND THEORETICAL MECHANISM

As shown in Fig. 1(a), the initial configuration consists of an interface between an isotropic dielectric medium and an untransformed uniaxial anisotropic medium. The upper half-space $y > 0$ is filled with an isotropic dielectric medium with permittivity $\varepsilon_1 > 0$, and the lower half-space $y < 0$ is initially filled with the untransformed uniaxial anisotropic medium. In its principal-axis frame, the in-plane permittivity tensor of the uniaxial medium is diagonal and expressed as $\hat{\varepsilon}_2 = \begin{pmatrix} \varepsilon_x & 0 \\ 0 & \varepsilon_y \end{pmatrix}$, where ε_x and ε_y are permittivity components along the x and y directions of the anisotropic uniaxial medium, respectively. The corresponding surface-mode field shown in Fig. 1(a) remains localized near the interface and exhibits exponential decay normal to the interface.

To introduce low-symmetry anisotropic coupling, a shear coordinate transformation is applied only to the lower anisotropic half-space, while the upper isotropic medium is left unchanged. The geometrical action of this transformation is illustrated in Fig. 1(c): the orthogonal coordinate grid in $y < 0$ is converted into a sheared grid, whereas the grid in $y > 0$ remains unchanged. The planar interface is kept fixed at $y = 0$. Therefore, the transformation modifies the constitutive parameters of the lower medium without bending or deforming the interface.

Following the transformation optics approach in [49], a shear transformation for the lower half-space is defined as $X = x$, $Y = y + tx$, and $Z = z$, where t is defined as the "shift parameter". While real-valued t has a direct geometrical interpretation as a real space shear, imaginary or complex-valued t is regarded here as an effective constitutive parametrization for constructing complex low-symmetry anisotropic media, rather than as a literal complex coordinate transformation. Under this half-space transformation, the original diagonal uniaxial permittivity tensor is converted into the effective low-symmetry tensor

$$\hat{\varepsilon} = \begin{pmatrix} 1 & 0 \\ t & 1 \end{pmatrix} \begin{pmatrix} \varepsilon_x & 0 \\ 0 & \varepsilon_y \end{pmatrix} \begin{pmatrix} 1 & t \\ 0 & 1 \end{pmatrix}$$

$$= \begin{pmatrix} \varepsilon_x & t\varepsilon_x \\ t\varepsilon_x & \varepsilon_y + t^2\varepsilon_x \end{pmatrix} = \begin{pmatrix} \varepsilon_{xx} & \varepsilon_{xy} \\ \varepsilon_{yx} & \varepsilon_{yy} \end{pmatrix}. \quad (1)$$

Correspondingly, the initially untilted surface-mode field evolves into a surface-bound field with oblique phase fronts inside the transformed medium. These tilted wavefronts arise from the transverse phase variation generated by the off-diagonal permittivity components. The transformed field propagates along the interface while simultaneously oscillating and decaying in the direction normal to the interface, as shown in Fig. 1(b). This combined oscillatory–evanescent behavior constitutes the characteristic ghost-wave response considered in this work.

To illustrate the surface-wave characteristics before transformation, Figs. 1(d)–(e) show magnetic-field distributions at interfaces between air and a uniaxial metal ($\varepsilon_x = -4$, $\varepsilon_y = -1$) and between air and a Type-II uniaxial hyperbolic medium ($\varepsilon_x = -2$, $\varepsilon_y = 4$), respectively, with $t = 0$. The field profiles correspond to a conventional surface plasmon polariton in Fig. 1(d) and a surface mode supported by the hyperbolic medium in Fig. 1(e). Both modes propagate along the interface while remaining confined to it, with their field amplitudes decaying exponentially away from the interface.

2.1. Dispersion Equation

Throughout this work, the time-harmonic convention $\exp(-\mathrm{i}\omega\tau)$ is adopted, where τ denotes time. A transverse-magnetic surface mode is assumed to propagate along the $+x$ direction and to remain confined to the interface. Its magnetic field is expressed as

$$H_z(x,y) = e^{\mathrm{i}k_x x}\begin{cases} Ae^{-\beta y} & (y>0) \\ Be^{\alpha y} & (y<0)\end{cases}, \tag{2}$$

where β is the decay constant in the isotropic medium, and α is the complex normal wavevector in the low-symmetry medium. The real and imaginary parts of α describe the attenuation and oscillation of the field along the negative y direction, respectively. According to the vector wave equation,

$$\nabla\times(\nabla\times\mathbf{E}) = \omega^2\mu_0\hat{\varepsilon}\cdot\mathbf{E}. \tag{3}$$

Substitution of the TM-polarized field into the wave equation yields the relations for β and α:

$$k_x^2-\beta^2 = k_0^2\varepsilon_1, \tag{4}$$

$$-\varepsilon_{xx}k_x^2+\varepsilon_{yy}\alpha^2+2\mathrm{i}\alpha\varepsilon_{xy}k_x+\left(\varepsilon_{xx}\varepsilon_{yy}-\varepsilon_{xy}^2\right)k_0^2=0. \tag{5}$$

The modal fields in the two half-spaces are connected through the boundary conditions at $y=0$. Since the shear transformation keeps the interface planar and fixed at $y=0$, and the tangential coordinate x remains continuous across the interface, the standard continuity conditions for the tangential electromagnetic fields remain applicable. Applying these conditions gives the surface-mode dispersion equation

$$\varepsilon_1\varepsilon_{yy}\alpha+\mathrm{i}\varepsilon_1\varepsilon_{xy}k_x-\left(\varepsilon_{xy}^2-\varepsilon_{xx}\varepsilon_{yy}\right)\beta=0. \tag{6}$$

2.2. Algebraic Solution

Having established the bulk-wave relations and the boundary-matching condition in Eqs. (4)–(6), we next solve the equations algebraically and identify the branches corresponding to physically admissible GSPs. We consider modes propagating along the $+x$ direction at the interface between the isotropic medium and the transformed low-symmetry medium.

For the field convention adopted in Eqs. (4) and (5), $\mathrm{Re}(k_x)>0$ is selected to represent phase propagation along $+x$. Surface confinement requires $\mathrm{Re}(\beta)>0$ in the upper isotropic half-space and $\mathrm{Re}(\alpha)>0$ in the lower anisotropic half-space. In addition, the ghost-wave character requires $\mathrm{Im}(\alpha)\neq 0$, so that the field simultaneously oscillates and decays in the direction normal to the interface. When k_x is complex, the non-growing branch along $+x$ further satisfies $\mathrm{Im}(k_x)\geq 0$ for the spatial factor $\exp(ik_x x)$.

Under these conditions, the solutions of Eqs. (4)–(6) can be written in algebraic form as

$$k_x = k_0\sqrt{\frac{-\varepsilon_x\varepsilon_y\varepsilon_1+(\varepsilon_y+t^2\varepsilon_x)\varepsilon_1^2}{\varepsilon_1^2-\varepsilon_x\varepsilon_y}}, \tag{7}$$

$$\alpha = \frac{-\varepsilon_x\varepsilon_y\beta-\mathrm{i}t\varepsilon_x\varepsilon_1k_x}{(\varepsilon_y+t^2\varepsilon_x)\varepsilon_1}, \tag{8}$$

$$\beta = k_0\sqrt{\frac{(\varepsilon_y+t^2\varepsilon_x-\varepsilon_1)\varepsilon_1^2}{\varepsilon_1^2-\varepsilon_x\varepsilon_y}}. \tag{9}$$

To describe the material parameter space in a compact form, we introduce the dimensionless permittivity ratio $m=\varepsilon_y/\varepsilon_x$, so that $\varepsilon_y=m\varepsilon_x$. The parameter space can therefore be represented by (ε_x,m). The denominator $\varepsilon_1^2-\varepsilon_x\varepsilon_y$ is assumed to be nonzero. The singular case $\varepsilon_1^2-\varepsilon_x\varepsilon_y=0$ corresponds to the curve $m=\varepsilon_1^2/\varepsilon_x^2$ in the (ε_x,m) parameter space, as indicated by the gray dashed line in Fig. 2. Along this curve, the analytical expressions in Eqs. (7)–(9) become singular. Therefore, this curve is excluded from the finite-parameter GSP existence domains discussed below.

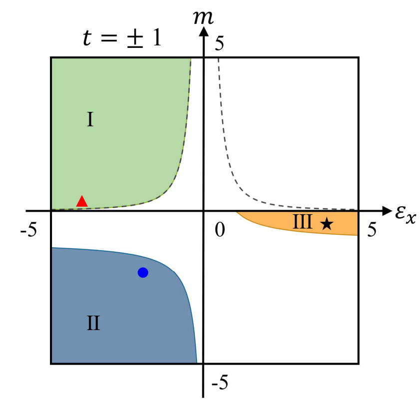

FIGURE 2. Existence domains of GSPs in the (ε_x,m) material parameter space for $t=\pm 1$, where $m=\varepsilon_y/\varepsilon_x$. The colored regions indicate the parameter domains satisfying the GSP existence conditions. The gray dashed line denotes the singular curve $\varepsilon_1^2-\varepsilon_x\varepsilon_y=0$, which is excluded from the finite-parameter GSP domains.

Equations (7)–(9) show explicitly that the longitudinal propagation constant and two transverse decay constants are jointly governed by the original principal permittivities and the shift parameter t. To examine the permitted material domains, the upper isotropic medium is taken to be air or vacuum ($\varepsilon_1=1$), and the signs of ε_x and ε_y are allowed to vary. The cases of real, imaginary, and general complex t are considered respectively.

It follows from Eqs. (7)–(9) that, when t is a non-zero real number, the existence condition of GSPs can be expressed as

$$\begin{cases} m>0, & \varepsilon_x<\frac{-\varepsilon_1}{\sqrt{m}} \\ m<0, & \begin{cases}\varepsilon_x>\frac{\varepsilon_1}{m+t^2}>0 \\ \varepsilon_x<\frac{\varepsilon_1}{m+t^2}<0\end{cases}\end{cases}. \tag{10}$$

For $t=\pm 1$, the resulting domains include transformed uniaxial metals (domain I), Type-I uniaxial hyperbolic media (domain III), and Type-II uniaxial hyperbolic media (domain II), as summarized in Fig. 2. The signs and magnitudes of the principal permittivities determine whether the solutions simultaneously satisfy surface confinement and transverse phase oscillation. When $t=0$, Eq. (8) gives $\mathrm{Im}(\alpha)=0$. The field in the anisotropic medium then decays without oscillation along the interface-normal direction. Consequently, the ghost-wave condition is not fulfilled, and the mode reduces to a conventional surface wave rather than a GSP.

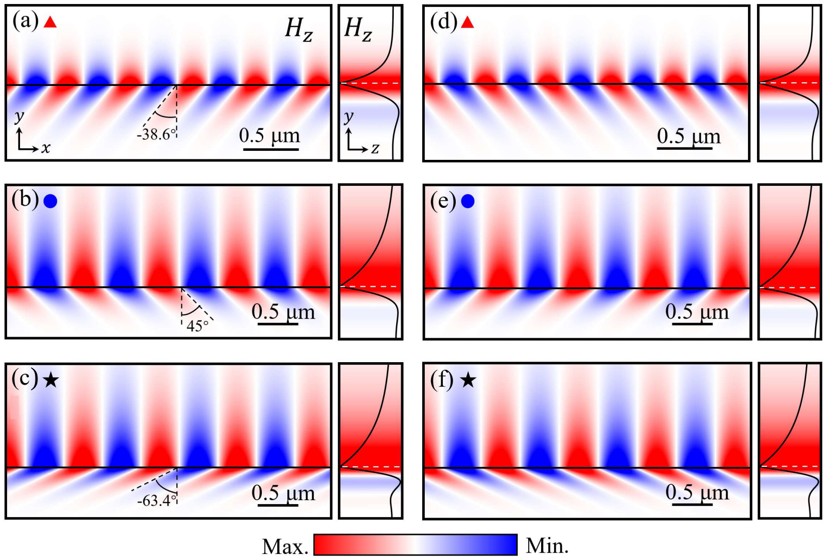

FIGURE 3. Analytical magnetic field distributions for the interface between air and a transformed anisotropic medium when the shift parameter t is a real number. (a)–(c) Cross-sectional near-field distributions, Re(H_z), of GSP modes propagating along the interface, with the corresponding field profiles in the y-z plane shown on the right. The solid black line denotes the interface at $y = 0$ between air and (a) a transformed uniaxial metal, (b) a transformed Type-II hyperbolic medium, (c) a transformed Type-I hyperbolic medium. The transformed material parameters are obtained with $t = 1$, and (d)–(f) same as (a)–(c), but for transformed material parameters obtained with $t = -1$. The material parameters of the transformed media correspond to the red triangle ($\varepsilon_x = -4$, $\varepsilon_y = -1$), blue circle ($\varepsilon_x = -2$, $\varepsilon_y = 4$), and black star ($\varepsilon_x = 4$, $\varepsilon_y = -2$) in Fig. 2.

3. NUMERICAL RESULTS AND DISCUSSION

Based on algebraic solutions and existence domains derived above, representative material parameters are selected from the allowed regions in Fig. 2 to examine the corresponding interfacial field distributions.

Figure 3 shows the cross-sectional magnetic-field distributions at interfaces between air and three transformed uniaxial media: a uniaxial metal, a Type-II hyperbolic medium, and a Type-I hyperbolic medium. The parameter sets correspond to the red triangle, blue circle, and black star in Fig. 2, respectively. For $t = 1$, Figs. 3(a)–(c) exhibit surface-bound fields with oblique wavefronts inside the transformed media. The fields decay away from the interface while simultaneously oscillating along the interface-normal direction, thereby confirming the ghost-wave character predicted by the analytical conditions. This mechanism differs from the GSPs caused by the optical axis tilting in the natural birefringent material calcite reported in previous studies [31]. Our approach is not limited to a specific material. Instead, GSP characteristics can be achieved by applying transformation optics to ordinary uniaxial materials, making the framework more general than previous studies.

When the shift parameter is changed from $t = 1$ to -1, the sign of the off-diagonal permittivity component is reversed. Consequently, the direction of the transverse phase variation is also reversed, as seen by comparing Figs. 3(a)–(c) with Figs. 3(d)–(f). The two sets of field maps therefore have opposite wavefront orientations while preserving their surface confinement and oscillatory-evanescent behavior. This result demonstrates that the sign of t controls the direction of the wavefront tilt, whereas its magnitude determines the strength of the induced shear-type anisotropic coupling.

For a real-valued shift parameter t, the wavefront tilt angle θ can be expressed analytically as a function of t (see the Appendix A for details):

$$\theta = \arctan\left(\frac{-t\varepsilon_x}{\varepsilon_y + t^2\varepsilon_x}\right), \qquad (11)$$

where θ is the angle between the wavefront and the y axis. To further illustrate the continuous tunability provided by t, Figs. A1 and A2 in Appendix A show the field distributions for several values of t (e.g., $t = 0.5$, 1, 1.5 and 2) in the transformed uniaxial metal and Type-II hyperbolic media, respectively. In both cases, the wavefront orientation varies continuously with t, although detailed dependence is determined by principal permittivities of the original uniaxial medium. This result provides a novel approach to high-precision light-field manipulation at the nanoscale and has potential for designing nanophotonic devices with directional propagation characteristics and anisotropic responses.

The preceding examples assume a real-valued t and lossless constituent parameters. To examine the influence of a complex-valued effective shift parameter, Figs. 4(a)–(c) present the corresponding field distributions for $t = 1 + 0.1\mathrm{i}$. The modes remain localized near the interface and retain the oblique wavefronts and simultaneous transverse oscillation and decay associated with ghost waves. However, k_x, α, and β generally become complex, and the field amplitude decreases along the $+x$ direction. Thus, the imaginary part of t modifies both the propagation attenuation and the normal field confinement, but it does not eliminate the basic ghost-wave character for the parameters considered here. A more detailed comparison of the modal characteristics and energy-transport properties for real

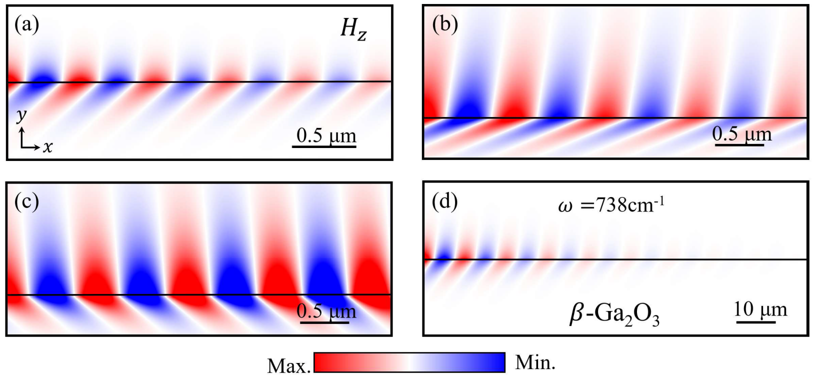

FIGURE 4. Analytical magnetic field distributions for the interface between air and transformed anisotropic media with a complex shift parameter t, and for the interface between air and natural low-symmetry medium β-Ga_2O_3. (a)–(c) Cross-sectional near-field distribution, $\mathrm{Re}(H_z)$, of a GSP mode propagating along the interface. The solid black line denotes the interface at $y = 0$ between air and (a) a transformed uniaxial metal ($\varepsilon_x = -4$, $\varepsilon_y = -1$), (b) a transformed Type-I hyperbolic medium ($\varepsilon_x = 4$, $\varepsilon_y = -2$), and (c) a transformed Type-II hyperbolic medium ($\varepsilon_x = -2$, $\varepsilon_y = 4$) with $t = 1 + 0.1\mathrm{i}$. (d) Near-field distribution of a GSP mode propagating along the interface between air and natural monoclinic β-Ga_2O_3 at a spectroscopic wavenumber of $738\,\mathrm{cm}^{-1}$. The permittivity tensor used for β-Ga_2O_3 is taken from [50], with $\varepsilon_{xx} = 1.04 + 1.96\mathrm{i}$, $\varepsilon_{yy} = 2.88 + 2.8\mathrm{i}$, and the off-diagonal component $\varepsilon_{xy} = \varepsilon_{yx} = 2.51 + 2.27\mathrm{i}$.

and complex-valued t, including the phase vector, attenuation vector, Poynting vector, propagation length, and penetration depths, is provided in Appendix A.

To show that the observed ghost-wave characteristics are not restricted to a limited class of natural crystals, Fig. 4(d) presents the analytical field distribution at the interface between air and natural monoclinic β-Ga_2O_3 at a spectroscopic wavenumber of $738\,\mathrm{cm}^{-1}$. The mode exhibits surface confinement together with oblique wavefront propagation inside the anisotropic medium. Because the permittivity tensor of β-Ga_2O_3 is complex at this frequency, the mode also attenuates along the propagation direction. This feature is consistent with the field profiles predicted for the effective low-symmetry medium obtained from a uniaxial medium when the shift parameter is complex. The similarity between this natural low-symmetry example and the complex t transformed media highlights that the ghost-wave behavior is associated with complex anisotropic coupling rather than with a single specific crystal.

Finally, the shift parameter is related to physically accessible effective anisotropic media. For real t, the required real off-diagonal response can be approached using an obliquely oriented subwavelength multilayer or another structured anisotropic medium. Reversing the layer tilt reverses the sign of the off-diagonal component and therefore corresponds to changing the sign of t. In realistic lossy multilayers, the effective diagonal and off-diagonal permittivity components are generally complex, providing a natural route for the complex t case. Appendix B gives a representative Cr-SiO_2 multilayer example and shows that the resulting effective medium supports an interfacial field with the same characteristic oblique and oscillatory–evanescent behavior. This implementation should be understood with the effective medium approximation, which requires the multilayer period to remain sufficiently smaller than the operating wavelength.

4. CONCLUSIONS

In this work, ghost surface polaritons are revisited from the perspective of transformation optics, and a transformation-optics-based approach is proposed to support them at isotropic–anisotropic interfaces using transformed uniaxial media. The analytical solutions and material-parameter conditions show that transformed uniaxial metals and hyperbolic media can support surface-bound modes with simultaneous oscillation and evanescent decay. The shift parameter provides an additional degree of freedom for controlling the wavefront orientation, while its complex extension further modifies the propagation attenuation and field confinement. Similar ghost-wave characteristics are also observed in natural monoclinic β-Ga_2O_3, further demonstrating that ghost surface modes are not restricted to a few specific natural crystals. Combined with the transformation-optics construction, this observation extends the accessible platforms for GSPs to a broader range of natural and engineered low-symmetry anisotropic media. Compared with relying on specific natural crystals, the transformation-optics approach provides greater flexibility in selecting the material platform and tailoring the effective anisotropy, wavefront orientation, and propagation characteristics. An obliquely stacked metal–dielectric multilayer is further presented as a possible effective medium realization of GSPs. This provides a complementary and designable route for supporting and controlling ghost surface modes, with potential applications in directional polariton routing, subwavelength wavefront shaping, near-field energy guiding, and anisotropic optical sensing.

ACKNOWLEDGEMENT

This work was supported by the National Natural Science Foundation of China (Grant Nos. 12404371 and 12361161667), the Guangdong Basic and Applied Basic Research Foundation (Grant No. 2024A1515011724), and the Shenzhen Science and Technology Program (Grant No. JCYJ20250604122934046).

APPENDIX A. CHARACTERISTICS AND ENERGY-TRANSPORT PROPERTIES OF GHOST SURFACE MODES

The relationship between the shift parameter and the GSP wavefront orientation can be obtained directly from the analytical surface-mode solution. In the transformed medium ($y < 0$), the magnetic field is written as

$$H_z = H_0 \exp\left(\mathrm{i}k_x x + \alpha y\right). \tag{A1}$$

Writing $k_x = \mathrm{Re}(k_x) + \mathrm{i}\mathrm{Im}(k_x)$ and $\alpha = \mathrm{Re}(\alpha) + \mathrm{i}\mathrm{Im}(\alpha)$, the field can be separated into amplitude and phase factors as

$$\begin{aligned} H_z &= H_0 \exp\left[-\mathrm{Im}\left(k_x\right) x + \mathrm{Re}\left(\alpha\right) y\right] \\ &\quad \times \exp\left\{\mathrm{i}\left[\mathrm{Re}\left(k_x\right) x + \mathrm{Im}\left(\alpha\right) y\right]\right\}. \end{aligned} \tag{A2}$$

Accordingly, the phase vector and attenuation vector in the transformed medium are $k_{ph} = \mathrm{Re}(k_x)\hat{x} + \mathrm{Im}(\alpha)\hat{y}$ and $\mathbf{k}_{\text{att}} = \mathrm{Im}(k_x)\hat{x} - \mathrm{Re}(\alpha)\hat{y}$, respectively, where the amplitude factor is written as $\exp(-k_{\text{att}} \cdot r)$. The phase vector is normal to the constant-phase wavefronts, whereas the attenuation vector specifies the direction of exponential amplitude decay.

For a real-valued shift parameter t in the lossless model, k_x is real, and the attenuation vector is directed purely normal to the interface. The nonzero transverse phase component $\mathrm{Im}(\alpha)$, together with $\mathrm{Re}(\alpha) > 0$, produces the simultaneous oscillation and evanescent decay characteristic of a ghost wave. The signed angle θ may be defined as the angle between the phase vector and the x axis, equivalently the angle between the wavefront and the y axis. Using $k_y = -\mathrm{i}\alpha$ and substituting Eqs. (7)–(9), one obtains $\theta = \arctan\left[\frac{\mathrm{Re}(k_y)}{\mathrm{Re}(k_x)}\right] = \arctan\left[\frac{\mathrm{Im}(\alpha)}{\mathrm{Re}(k_x)}\right]$, and therefore

$$\theta = \arctan\left(\frac{-t\varepsilon_x}{\varepsilon_y + t^2\varepsilon_x}\right). \tag{A3}$$

Equation (A3) has a direct geometrical interpretation only when t is real. For complex-valued t, the modal wavevector components are generally complex, and the phase-front orientation must instead be determined from the real components of the phase vector, rather than by directly substituting a complex t into Eq. (A3).

Figure A1 shows the cross-sectional magnetic-field distributions at the air-transformed-medium interface for a transformed uniaxial metal with $\varepsilon_x = -4$ and $\varepsilon_y = -1$. As t increases from 0.5 to 2, the wavefront angle changes continuously from -45° to -25.1°, in agreement with Eq. (A3). The field remains localized near the interface while exhibiting oscillatory and evanescent behavior inside the transformed medium. Fig. A2 presents the corresponding results for a transformed Type-II uniaxial hyperbolic medium with $\varepsilon_x = -2$ and $\varepsilon_y = 10$. In this case, the wavefront angle increases from 6° to 63.4° over the same range of t. The different angular trends in Figs. A1 and A2 arise from their different principal permittivities, whereas both sets of results demonstrate that the shift parameter continuously controls the internal phase-front orientation.

The influence of a complex shift parameter on propagation attenuation, field confinement, and energy transport is illustrated in Fig. A3. For real-valued t in the lossless model, $\mathrm{Im}(k_x) = 0$, and the mode does not attenuate along the propagation direction. When t becomes complex, k_x, α, and β generally become complex. The real part $\mathrm{Re}(k_x)$ determines phase propagation along the interface, whereas $\mathrm{Im}(k_x)$ produces exponential attenuation along the x direction. The field-amplitude propagation length is therefore defined as $L_{\text{amp}} = 1/|\mathrm{Im}(k_x)|$, and the corresponding field-amplitude penetration depths in the upper isotropic medium and lower anisotropic medium are $\delta_{\text{air}}^{\text{amp}} = 1/|\mathrm{Re}(\beta)|$ and $\delta_{\text{aniso}}^{\text{amp}} = 1/|\mathrm{Re}(\alpha)|$.

The associated intensity propagation length and intensity penetration depths are one half of the amplitude-based values. For $t = 1$, the lossless model gives an infinite propagation length, whereas $t = 1 + 0.1\mathrm{i}$ produces a finite propagation length and modifies the penetration depths on both sides of the interface, as indicated in Figs. A3(a) and A3(b).

The time-averaged energy-flow direction is characterized by the Poynting vector as specified in Eq. (A4).

$$\mathbf{S} = \frac{1}{2}\mathrm{Re}\left(\mathbf{E} \times \mathbf{H}^*\right) \tag{A4}$$

For the TM-polarized modes considered here, $\mathbf{H} = (0, 0, H_z)$ and $\mathbf{E} = (E_x, E_y, 0)$, so that

$$S_x = \frac{1}{2}\mathrm{Re}\left(E_y H_z^*\right), \quad S_y = -\frac{1}{2}\mathrm{Re}\left(E_x H_z^*\right). \tag{A5}$$

As shown in Fig. A3(a), for the real-valued case $t = 1$, the phase vector is tilted inside the anisotropic medium, and the attenuation vector remains normal to the interface because k_x is real in the lossless model. The Poynting vector is not parallel to the phase vector, reflecting the difference between phase propagation and energy transport. For $t = 1 + 0.1\mathrm{i}$, as shown in Fig. A3(b), the attenuation vector acquires a tangential component due to the nonzero $\mathrm{Im}(k_x)$, resulting in a finite propagation length along the interface. The corresponding changes in the penetration depths are also indicated in the field distribution.

The normalized interface-field amplitudes $|H_z(x,0)|/|H_z(0,0)|$ for $t = 1$ and $t = 1 + 0.1\mathrm{i}$ are compared in Fig. A3(c). The amplitude remains constant for real t in the lossless model, whereas it decreases exponentially for complex t because $\mathrm{Im}(k_x)$ is nonzero. Thus, the imaginary component of the shift parameter introduces propagation attenuation while the mode retains its oblique wavefronts and oscillatory-evanescent behavior inside the anisotropic medium. The complex shift parameter therefore modifies both the propagation length along the interface and the field confinement normal to it without eliminating the ghost-wave character.

APPENDIX B. A POSSIBLE PHYSICAL REALIZATION OF GHOST SURFACE MODES

A possible physical realization of ghost surface modes can be achieved using an obliquely stacked A–B multilayer, as illustrated in Fig. B1(a). When the multilayer period is much smaller than the operating wavelength, the structure can be described within the effective medium approximation as a homogeneous anisotropic medium. Although the effective permit-

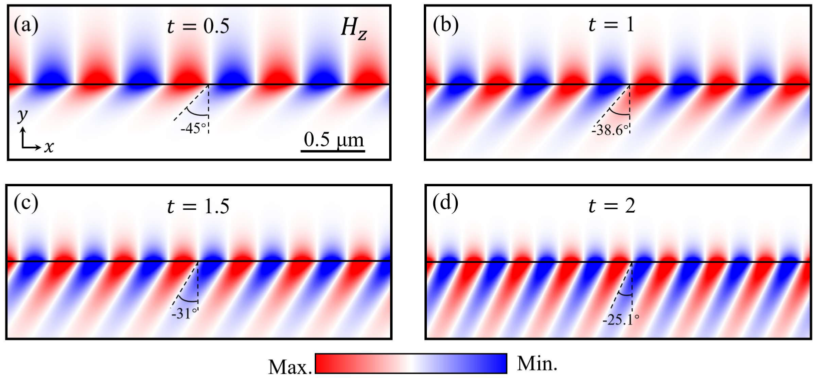

FIGURE A1. (a)–(d) Cross-sectional magnetic-field distributions, $\mathrm{Re}(H_z)$, of GSPs at the air-transformed medium interface for a transformed uniaxial metal ($\varepsilon_x = -4$, $\varepsilon_y = -1$) with $t = 0.5$, 1, 1.5, and 2. The solid black line denotes the interface at $y = 0$.

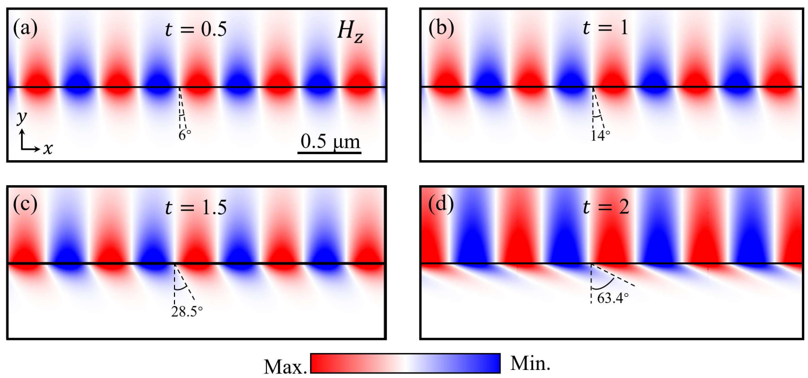

FIGURE A2. (a)–(d) Cross-sectional magnetic-field distributions, $\mathrm{Re}(H_z)$, of GSPs at the air-transformed medium interface for a transformed Type-II uniaxial hyperbolic medium ($\varepsilon_x = -2$, $\varepsilon_y = 10$) with $t = 0.5$, 1, 1.5, and 2, respectively. The solid black line denotes the interface at $y = 0$.

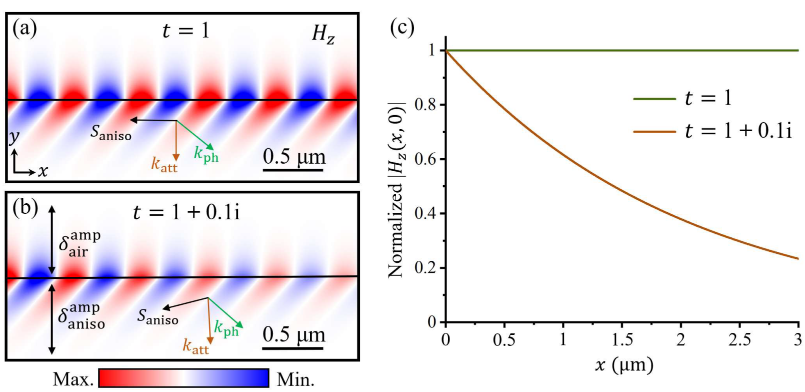

FIGURE A3. Effect of a complex shift parameter on the propagation attenuation, field confinement, and energy transport of GSP-like modes. (a)–(b) Cross-sectional magnetic-field distributions, $\mathrm{Re}(H_z)$, for the transformed uniaxial metal with $\varepsilon_x = -4$, $\varepsilon_y = -1$, and $\varepsilon_1 = 1$, corresponding to $t = 1$ and $t = 1 + 0.1\mathbf{i}$, respectively. The arrows indicate the phase vector k_{ph}, attenuation vector k_{att}, and time-averaged Poynting vector $\mathbf{S}_{\mathrm{aniso}}$ in the anisotropic medium. (c) Normalized interface-field amplitude $|H_z(x, 0)| \,/\, |H_z(0, 0)|$, showing the propagation attenuation induced by the imaginary component of t.

tivity tensor is diagonal in the principal-axis frame of the multilayer, tilting the layers with respect to the interface produces nonzero off-diagonal components when the tensor is expressed in the interface-based x-y coordinate system. The strength and sign of this anisotropic coupling can be controlled via the constituent permittivities, filling fraction f, and tilt angle φ.

As a representative example, an obliquely stacked Cr-SiO_2 multilayer with a period of $a = 100\,\mathrm{nm}$ is considered the lower effective anisotropic medium, while an isotropic SiO_2 medium occupies the upper half-space. When the multilayer period is much smaller than the operating wavelength, its effective permittivities parallel and perpendicular to the layers can be writ-

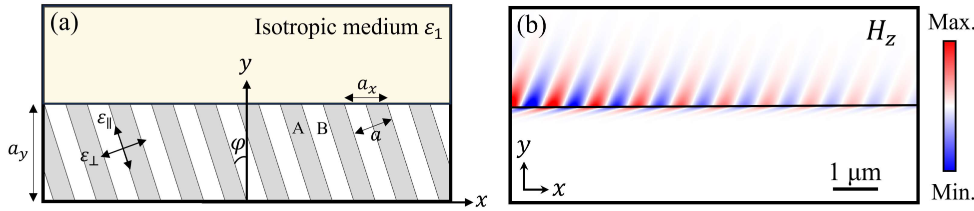

FIGURE B1. (a) Schematic of the interface between an isotropic medium and an obliquely stacked A–B multilayer. The multilayer period and tilt angle are denoted by a and φ, respectively. The period in the x direction is given by $a_x = a/\cos\varphi$, and the period in the y direction is given by $a_y = a/\sin\varphi$. The structure is uniform along the z direction. (b) Cross-sectional magnetic-field distribution, $\mathrm{Re}(H_z)$, at the interface between isotropic SiO_2 medium and the effective anisotropic medium formed by the obliquely stacked Cr-SiO_2 multilayer. The permittivity of Cr is assumed to be $\varepsilon_{\mathrm{Cr}} = \varepsilon_{\mathrm{A}} = -3.072 + 29.929\mathrm{i}$ [51], and the permittivity of SiO_2 is taken as $\varepsilon_{\mathrm{SiO_2}} = \varepsilon_1 = \varepsilon_{\mathrm{B}} = 2.08$ [52] at a wavelength of 1500 nm. The Cr filling fraction and tilt angle are $f = 0.9$ and $\varphi = 60^\circ$, respectively.

ten as $\varepsilon_\parallel = f\varepsilon_{\mathrm{Cr}} + (1-f)\varepsilon_{\mathrm{SiO_2}}$ and $\frac{1}{\varepsilon_\perp} = \frac{f}{\varepsilon_{\mathrm{Cr}}} + \frac{1-f}{\varepsilon_{\mathrm{SiO_2}}}$, respectively. For $\varepsilon_{\mathrm{Cr}} = -3.072 + 29.929\mathrm{i}$, $\varepsilon_{\mathrm{SiO_2}} = 2.08$ and $f = 0.9$ at a wavelength of 1500 nm, these components are obtained as $\varepsilon_\parallel = -2.557 + 26.936\mathrm{i}$, $\varepsilon_\perp = 15.458 + 10.217\mathrm{i}$. After the multilayer is tilted by $\varphi = 60^\circ$, the effective permittivity tensor in the interface-based coordinate system becomes $\varepsilon_{xx} = 1.947 + 22.756\mathrm{i}$, $\varepsilon_{xy} = 7.8 - 7.24\mathrm{i}$, $\varepsilon_{yy} = 10.954 + 14.397\mathrm{i}$. By expressing the in-plane tensor in the same algebraic form as the transformation-optics tensor, the corresponding effective shift parameter is $t_{\mathrm{eff}} = -0.287 - 0.367\mathrm{i}$.

The complex permittivity of Cr introduces material loss into the multilayer and consequently makes both the diagonal and off-diagonal components of the effective permittivity tensor complex. Therefore, this configuration provides a representative realization of the complex-valued t case discussed in the main text.

Figure B1(b) shows the corresponding analytical surface-mode field at the interface. The field remains confined to the interface and exhibits oblique phase fronts together with simultaneous oscillation and decay inside the effective anisotropic medium. These features are characteristic of a ghost surface mode. Owing to the material loss, the propagation constant along the interface is also complex, leading to attenuation of the mode during propagation. This example therefore demonstrates that the field characteristics for complex t, including tilted wavefronts, oscillatory decay normal to the interface, and finite propagation length, can in principle be reproduced using a lossy tilted multilayer platform. In practical implementations, the operating bandwidth is limited by the dispersion and loss of the constituent materials and by the frequency range over which the effective medium approximation remains valid. Fabrication deviations in the layer thicknesses, filling fraction, tilt angle, and constituent parameters may modify the effective permittivity tensor, thereby affecting the phase-front inclination, propagation length, and field confinement of the ghost surface mode. A quantitative evaluation of these effects depends on the specific material platform and fabrication process. Nevertheless, the proposed tilted multilayer provides a possible effective medium platform for reproducing the characteristic field behavior of ghost surface modes.

REFERENCES

[1] Dai, S., Z. Fei, Q. Ma, A. S. Rodin, M. Wagner, A. S. McLeod, M. K. Liu, W. Gannett, W. Regan, *et al.*, "Tunable phonon polaritons in atomically thin van der Waals crystals of boron nitride," *Science*, Vol. 343, No. 6175, 1125–1129, 2014.

[2] Dai, S., Q. Ma, T. Andersen, A. S. Mcleod, Z. Fei, M. K. Liu, M. Wagner, K. Watanabe, T. Taniguchi, M. Thiemens, F. Keilmann, P. Jarillo-Herrero, M. M. Fogler, and D. N. Basov, "Subdiffractional focusing and guiding of polaritonic rays in a natural hyperbolic material," *Nature Communications*, Vol. 6, No. 1, 6963, 2015.

[3] Ma, W., P. Alonso-González, S. Li, A. Y. Nikitin, J. Yuan, J. Martín-Sánchez, J. Taboada-Gutiérrez, I. Amenabar, P. Li, S. Vélez, C. Tollan, Z. Dai, Y. Zhang, S. Sriram, K. Kalantar-Zadeh, S.-T. Lee, R. Hillenbrand, and Q. Bao, "In-plane anisotropic and ultra-low-loss polaritons in a natural van der Waals crystal," *Nature*, Vol. 562, No. 7728, 557–562, 2018.

[4] Li, P., I. Dolado, F. J. Alfaro-Mozaz, F. Casanova, L. E. Hueso, S. Liu, J. H. Edgar, A. Y. Nikitin, S. Vélez, and R. Hillenbrand, "Infrared hyperbolic metasurface based on nanostructured van der Waals materials," *Science*, Vol. 359, No. 6378, 892–896, 2018.

[5] Caldwell, J. D., A. V. Kretinin, Y. Chen, V. Giannini, M. M. Fogler, Y. Francescato, C. T. Ellis, J. G. Tischler, C. R. Woods, A. J. Giles, *et al.*, "Sub-diffractional volume-confined polaritons in the natural hyperbolic material hexagonal boron nitride," *Nature Communications*, Vol. 5, No. 1, 5221, 2014.

[6] Yuan, Z., R. Chen, P. Li, A. Y. Nikitin, R. Hillenbrand, and X. Zhang, "Extremely confined acoustic phonon polaritons in monolayer-hBN/metal heterostructures for strong light-matter interactions," *ACS Photonics*, Vol. 7, No. 9, 2610–2617, 2020.

[7] Lyu, W., H. Teng, C. Wu, X. Zhang, X. Guo, X. Yang, and Q. Dai, "Anisotropic acoustic phonon polariton-enhanced infrared spectroscopy for single molecule detection," *Nanoscale*, Vol. 13, No. 29, 12 720–12 726, 2021.

[8] Pérez, Álvarez G., T. G. Folland, I. Errea, J. Taboada-Gutiérrez, J. Duan, J. Martín-Sánchez, A. I. F. Tresguerres-Mata, J. R. Matson, A. Bylinkin, M. He, W. Ma, Q. Bao, J. I. Martín, J. D. Caldwell, A. Y. Nikitin, and P. Alonso-González, "Infrared permittivity of the biaxial van der Waals semiconductor α-MoO_3 from near- and far-field correlative studies," *Advanced Materials*, Vol. 32, No. 29, 1908176, 2020.

[9] Wu, Y., J. Duan, W. Ma, Q. Ou, P. Li, P. Alonso-González, J. D. Caldwell, and Q. Bao, "Manipulating polaritons at the extreme scale in van der Waals materials," *Nature Reviews Physics*, Vol. 4, No. 9, 578–594, 2022.

[10] Li, P., M. Lewin, A. V. Kretinin, J. D. Caldwell, K. S. Novoselov, T. Taniguchi, K. Watanabe, F. Gaussmann, and T. Taubner, "Hyperbolic phonon-polaritons in boron nitride for near-field optical imaging and focusing," *Nature Communications*, Vol. 6, No. 1, 7507, 2015.

[11] Li, P., I. Dolado, F. J. Alfaro-Mozaz, A. Y. Nikitin, F. Casanova, L. E. Hueso, S. Vélez, and R. Hillenbrand, "Optical nanoimaging of hyperbolic surface polaritons at the edges of van der Waals materials," *Nano Letters*, Vol. 17, No. 1, 228–235, 2017.

[12] Martín-Sánchez, J., J. Duan, J. Taboada-Gutiérrez, G. Álvarez Pérez, K. V. Voronin, I. Prieto, W. Ma, Q. Bao, *et al.*, "Focusing of in-plane hyperbolic polaritons in van der Waals crystals with tailored infrared nanoantennas," *Science Advances*, Vol. 7, No. 41, eabj0127, 2021.

[13] Zheng, Z., J. Jiang, N. Xu, X. Wang, W. Huang, Y. Ke, S. Zhang, H. Chen, and S. Deng, "Controlling and focusing in-plane hyperbolic phonon polaritons in α-MoO_3 with a curved plasmonic antenna," *Advanced Materials*, Vol. 34, No. 6, 2104164, 2022.

[14] He, M., G. R. S. Iyer, S. Aarav, S. S. Sunku, A. J. Giles, T. G. Folland, N. Sharac, X. Sun, J. Matson, S. Liu, J. H. Edgar, J. W. Fleischer, D. N. Basov, and J. D. Caldwell, "Ultrahigh-resolution, label-free hyperlens imaging in the mid-IR," *Nano Letters*, Vol. 21, No. 19, 7921–7928, 2021.

[15] Folland, T. G., A. Fali, S. T. White, J. R. Matson, S. Liu, N. A. Aghamiri, J. H. Edgar, R. F. Haglund Jr., Y. Abate, and J. D. Caldwell, "Reconfigurable infrared hyperbolic metasurfaces using phase change materials," *Nature Communications*, Vol. 9, No. 1, 4371, 2018.

[16] Chaudhary, K., M. Tamagnone, X. Yin, C. M. Spägele, S. L. Oscurato, J. Li, C. Persch, R. Li, N. A. Rubin, L. A. Jauregui, K. Watanabe, T. Taniguchi, P. Kim, M. Wuttig, J. H. Edgar, A. Ambrosio, and F. Capasso, "Polariton nanophotonics using phase-change materials," *Nature Communications*, Vol. 10, No. 1, 4487, 2019.

[17] Zheng, Z., N. Xu, S. L. Oscurato, M. Tamagnone, F. Sun, Y. Jiang, Y. Ke, J. Chen, W. Huang, W. L. Wilson, *et al.*, "A mid-infrared biaxial hyperbolic van der Waals crystal," *Science Advances*, Vol. 5, No. 5, eaav8690, 2019.

[18] Ni, G. X., H. Wang, B.-Y. Jiang, L. X. Chen, Y. Du, Z. Y. Sun, M. D. Goldflam, A. J. Frenzel, X. M. Xie, M. M. Fogler, and D. N. Basov, "Soliton superlattices in twisted hexagonal boron nitride," *Nature Communications*, Vol. 10, No. 1, 4360, 2019.

[19] Hu, G., Q. Ou, G. Si, Y. Wu, J. Wu, Z. Dai, A. Krasnok, Y. Mazor, Q. Zhang, Q. Bao, C.-W. Qiu, and A. Alù, "Topological polaritons and photonic magic angles in twisted α-MoO_3 bilayers," *Nature*, Vol. 582, No. 7811, 209–213, 2020.

[20] Chen, M., X. Lin, T. H. Dinh, Z. Zheng, J. Shen, Q. Ma, H. Chen, P. Jarillo-Herrero, and S. Dai, "Configurable phonon polaritons in twisted α-MoO_3," *Nature Materials*, Vol. 19, No. 12, 1307–1311, 2020.

[21] Duan, J., N. Capote-Robayna, J. Taboada-Gutiérrez, G. Álvarez Pérez, I. Prieto, J. Martín-Sánchez, A. Y. Nikitin, and P. Alonso-González, "Twisted nano-optics: Manipulating light at the nanoscale with twisted phonon polaritonic slabs," *Nano Letters*, Vol. 20, No. 7, 5323–5329, 2020.

[22] Zheng, Z., F. Sun, W. Huang, J. Jiang, R. Zhan, Y. Ke, H. Chen, and S. Deng, "Phonon polaritons in twisted double-layers of hyperbolic van der Waals crystals," *Nano Letters*, Vol. 20, No. 7, 5301–5308, 2020.

[23] Duan, J., G. Álvarez Pérez, C. Lanza, K. Voronin, A. I. F. Tresguerres-Mata, N. Capote-Robayna, J. Álvarez Cuervo, A. T. Martín-Luengo, J. Martín-Sánchez, V. S. Volkov, A. Y. Nikitin, and P. Alonso-González, "Multiple and spectrally robust photonic magic angles in reconfigurable α-MoO_3 trilayers," *Nature Materials*, Vol. 22, No. 7, 867–872, 2023.

[24] Alfaro-Mozaz, F. J., P. Alonso-González, S. Vélez, I. Dolado, M. Autore, S. Mastel, F. Casanova, L. E. Hueso, P. Li, A. Y. Nikitin, and R. Hillenbrand, "Nanoimaging of resonating hyperbolic polaritons in linear boron nitride antennas," *Nature Communications*, Vol. 8, No. 1, 15624, 2017.

[25] Barcelos, I. D., T. A. Canassa, R. A. Mayer, F. H. Feres, E. G. de Oliveira, A.-M. B. Goncalves, H. A. Bechtel, R. O. Freitas, F. C. B. Maia, and D. C. B. Alves, "Ultrabroadband nanocavity of hyperbolic phonon–polaritons in 1D-like α-MoO_3," *ACS Photonics*, Vol. 8, No. 10, 3017–3026, 2021.

[26] Kim, S., J. E. Fröch, J. Christian, M. Straw, J. Bishop, D. Totonjian, K. Watanabe, T. Taniguchi, M. Toth, and I. Aharonovich, "Photonic crystal cavities from hexagonal boron nitride," *Nature Communications*, Vol. 9, No. 1, 2623, 2018.

[27] Calandrini, E., K. Voronin, O. Balci, M. Barra-Burillo, A. Bylinkin, S. M. Shinde, S. Sharma, F. Casanova, L. E. Hueso, A. Chuvilin, C. McAleese, B. R. Conran, X. Wang, K. Teo, V. S. Volkov, A. C. Ferrari, A. Y. Nikitin, and R. Hillenbrand, "Near- and far-field observation of phonon polaritons in wafer-scale multilayer hexagonal boron nitride prepared by chemical vapor deposition," *Advanced Materials*, Vol. 35, No. 44, 2302045, 2023.

[28] Dai, S., M. Tymchenko, Y. Yang, Q. Ma, M. Pita-Vidal, K. Watanabe, T. Taniguchi, P. Jarillo-Herrero, M. M. Fogler, A. Alù, and D. N. Basov, "Manipulation and steering of hyperbolic surface polaritons in hexagonal boron nitride," *Advanced Materials*, Vol. 30, No. 16, 1706358, 2018.

[29] Fei, Z., A. S. Rodin, G. O. Andreev, W. Bao, A. S. McLeod, M. Wagner, L. M. Zhang, Z. Zhao, M. Thiemens, G. Dominguez, M. M. Fogler, A. H. C. Neto, C. N. Lau, F. Keilmann, and D. N. Basov, "Gate-tuning of graphene plasmons revealed by infrared nano-imaging," *Nature*, Vol. 487, No. 7405, 82–85, 2012.

[30] Chen, J., M. Badioli, P. Alonso-González, S. Thongrattanasiri, F. Huth, J. Osmond, M. Spasenović, A. Centeno, A. Pesquera, P. Godignon, A. Z. Elorza, N. Camara, F. J. G. de Abajo, R. Hillenbrand, and F. H. L. Koppens, "Optical nano-imaging of gate-tunable graphene plasmons," *Nature*, Vol. 487, No. 7405, 77–81, 2012.

[31] Ma, W., G. Hu, D. Hu, R. Chen, T. Sun, X. Zhang, Q. Dai, Y. Zeng, A. Alù, C.-W. Qiu, and P. Li, "Ghost hyperbolic surface polaritons in bulk anisotropic crystals," *Nature*, Vol. 596, No. 7872, 362–366, 2021.

[32] Narimanov, E. E., "Dyakonov waves in biaxial anisotropic crystals," *Physical Review A*, Vol. 98, No. 1, 013818, 2018.

[33] Narimanov, E. E., "Ghost resonance in anisotropic materials: Negative refractive index and evanescent field enhancement in lossless media," *Advanced Photonics*, Vol. 1, No. 4, 046003, 2019.

[34] Wu, K., P. Coquet, Q. J. Wang, and P. Genevet, "Modelling of free-form conformal metasurfaces," *Nature Communications*, Vol. 9, No. 1, 3494, 2018.

[35] Lebbe, N., S. Lanteri, S. Y. Golla, and P. Genevet, "Susceptibility synthesis of arbitrary shaped metasurfaces," *Physical Review B*, Vol. 106, No. 3, 035110, 2022.

[36] Leonhardt, U., "Optical conformal mapping," *Science*, Vol. 312, No. 5781, 1777–1780, 2006.

[37] Pendry, J. B., D. Schurig, and D. R. Smith, "Controlling electromagnetic fields," *Science*, Vol. 312, No. 5781, 1780–1782, 2006.

[38] Chen, H., C. T. Chan, and P. Sheng, "Transformation optics and metamaterials," *Nature Materials*, Vol. 9, No. 5, 387–396, 2010.

[39] Schurig, D., J. J. Mock, B. J. Justice, S. A. Cummer, J. B. Pendry, A. F. Starr, and D. R. Smith, "Metamaterial electromagnetic cloak at microwave frequencies," *Science*, Vol. 314, No. 5801, 977–980, 2006.

[40] Chen, H. and C. T. Chan, "Transformation media that rotate electromagnetic fields," *Applied Physics Letters*, Vol. 90, No. 24, 241105, 2007.

[41] Chen, H., B. Hou, S. Chen, X. Ao, W. Wen, and C. T. Chan, "Design and experimental realization of a broadband transformation media field rotator at microwave frequencies," *Physical Review Letters*, Vol. 102, No. 18, 183903, 2009.

[42] Sadeghi, M. M., S. Li, L. Xu, B. Hou, and H. Chen, "Transformation optics with Fabry-Pérot resonances," *Scientific Reports*, Vol. 5, No. 1, 8680, 2015.

[43] Xu, Y., S. Du, L. Gao, and H. Chen, "Overlapped illusion optics: A perfect lens brings a brighter feature," *New Journal of Physics*, Vol. 13, No. 2, 023010, 2011.

[44] Jiang, W. X., C.-W. Qiu, T. Han, S. Zhang, and T. J. Cui, "Creation of ghost illusions using wave dynamics in metamaterials," *Advanced Functional Materials*, Vol. 23, No. 32, 4028–4034, 2013.

[45] Lai, Y., J. Ng, H. Chen, D. Han, J. Xiao, Z.-Q. Zhang, and C. T. Chan, "Illusion optics: The optical transformation of an object into another object," *Physical Review Letters*, Vol. 102, No. 25, 253902, 2009.

[46] Li, C., X. Meng, X. Liu, F. Li, G. Fang, H. Chen, and C. T. Chan, "Experimental realization of a circuit-based broadband illusion-optics analogue," *Physical Review Letters*, Vol. 105, No. 23, 233906, 2010.

[47] Gabrielli, L. H., D. Liu, S. G. Johnson, and M. Lipson, "On-chip transformation optics for multimode waveguide bends," *Nature Communications*, Vol. 3, No. 1, 1217, 2012.

[48] Badri, S. H., H. R. Saghai, and H. Soofi, "Polygonal Maxwell's fisheye lens via transformation optics as multimode waveguide crossing," *Journal of Optics*, Vol. 21, No. 6, 065102, 2019.

[49] Chen, H. and C. T. Chan, "Electromagnetic wave manipulation by layered systems using the transformation media concept," *Physical Review B*, Vol. 78, No. 5, 054204, 2008.

[50] Passler, N. C., X. Ni, G. Hu, J. R. Matson, G. Carini, M. Wolf, M. Schubert, A. Alù, J. D. Caldwell, T. G. Folland, and A. Paarmann, "Hyperbolic shear polaritons in low-symmetry crystals," *Nature*, Vol. 602, No. 7898, 595–600, 2022.

[51] Yoda, T., Y. Moritake, K. Takata, K. Yokomizo, S. Murakami, and M. Notomi, "Optical non-Hermitian skin effect in uniform media," *Physical Review Research*, Vol. 7, No. 3, 033214, 2025.

[52] Malitson, I. H., "Interspecimen comparison of the refractive index of fused silica," *Journal of the Optical Society of America*, Vol. 55, No. 10, 1205–1209, 1965.